Astronomy & Astrophysics manuscript no. HD210684_aa
January 1, 2026

Study of photometric and spectral variability of the roAp star HD 210684

V. Khalack[1] and C. Lovekin[2]

[1] Département de Physique et d'Astronomie, Université de Moncton, Moncton, N.B., Canada E1A 3E9
e-mail: Viktor.Khalack@umoncton.ca
[2] Department of Physics, Mount Allison University, Sackville, N.B., Canada E4L 1E6

Received January 1?, 2026

ABSTRACT

Aims. This paper studies photometric and spectropolarimetric variability of HD 210684 in order to derive its magnetic properties, rotational period, evolutionary stage, and global stellar parameters.
Methods. The discrete Fourier Transform and Lomb-Scargle periodograms are used to measure frequencies and amplitudes of periodic signals present in light curves of HD 210684. Evolution models are calculated with MESA, while roAp type pulsations are simulated with GYRE. The values of $T_{\rm eff}$, $\log(g)$, $v\sin i$, and radial velocity (RV) are derived from the best fit of Balmer line profiles using FITSB2. The Least Square Deconvolution (LSD) method is applied to available Stokes I & V spectra to measure the mean longitudinal magnetic field $\langle B_z \rangle$ and RV.
Results. Detailed analysis of photometric variability of the light curves provided by *TESS* for HD 210684 reveals rotational modulation with period P=5.02188±0.00005 d and splitting of high-overtone pulsations that corresponds to a significantly smaller rotational period at the layer of generation of pulsational instability, which suggests angular momentum transfer. Derived $\langle B_z \rangle$ measurements also show periodic variability with P=5.02188 d, but this variability appears to be different from the one predicted by a centered magnetic dipole model, suggesting that the configuration of the surface magnetic field is more complex than the dipolar one. We have determined the inclination angle between the line of sight and the rotation axis to be $i = 31.2^\circ \pm 1.8^\circ$, and the angle between the rotation and magnetic dipole axes as $\beta = 77^\circ \pm 3^\circ$. Simulations of stellar pulsations constrain $\log T_{\rm eff} < 3.85$ and show that our best fitting model depends on whether the observed modes are $\ell = 1$ or $\ell = 2$.
Conclusions. Considering the derived value of β, we prefer the best fit model with $\ell = 2$ mode, which predicts that HD 210684 lies on the main sequence with an age of approximately 1.45 Gyr. Meanwhile, only the most evolved and coolest models in our grid show $\eta > 0$ (when frequencies are driven) for the observed triplet. The best fit of Balmer line profiles has resulted in higher values of $T_{\rm eff}$ and $\log(g)$ for spectra acquired at rotational phases φ= 0.14 – 0.39 suggesting visibility of an area with higher surface temperature. Strong asymmetry of the LSD Stokes I profiles derived at φ= 0.307 and 0.394 supports this hypothesis. Clear variability of the LSD Stokes I profiles with rotational phase argues for horizontal abundance stratification that may be linked to the inhomogenity of surface temperature. Further spectropolarimetric observations of HD 210684 are required to study its unique properties in detail.

Key words. stars: chemically peculiar – stars: magnetic field – stars: rotation – stars: oscillations – stars: individual: HD 210684

1. Introduction

The Transiting Exoplanet Survey Satellite (*TESS*) (Ricker et al. 2015) launched in April of 2018, has collected a huge amount of high-quality photometric data for stellar targets located over the whole sky during the 7 last years of its operation. Extensive analysis of the *TESS* data provided by Mikulski Archive for Space Telescopes[1] (MAST) allowed to discover new candidate roAp stars (see for example Mathys et al. 2023) and confirm the presence of high-overtone pulsations in the known roAp stars located in Southern (using the cycle-1 data) (Holdsworth et al. 2021) and Northern (using the cycle-2 data) (Holdsworth et al. 2024) hemispheres. HD 210684 was first identified as a roAp type candidate by O. Kobzar in 2020 with rotational modulation (P = 5.04±0.02 d) during the analysis of the cycle-2 data for his master's thesis. Since 2020, regular spectropolarimetric observations of this target have been carried out at the Canada-France-Hawaii Telescope (CFHT) to accumulate Stoke I & V spectra suitable for abundance analysis and for measurements of magnetic field, which is expected to be found in the roAp stars.

HD 210684 (HIP 109552, TIC 259017938) is located 142.71±0.46 pc from our Sun (Brandt 2021) and according to Cannon & Pickering (1993) has been assigned a spectral type F0. By studying its long-term proper motion in the Hipparcos data and Gaia's second data release (GDR2) catalogs Kervella et al. (2019) have detected a proper motion anomaly consistent with the presence of a perturbing secondary object of mass M=79.35±9.63 M_J located at distance around 1.89 A.U. from the primary. Balona (2022) has reported a detection of rotational modulation with period P = 5.102 d in the *TESS* light curve of HD 210684 and marked it as a probable roAp candidate. Based on the clear detection of the high-overtone pulsations at 1.352116 mHz, Holdsworth et al. (2024) have confirmed its roAp nature.

In this article, we aim to carry out an extensive analysis of the available data for the recently discovered roAp variable HD 210684. We combine its *TESS* photometric data with high-resolution Stokes I & V spectra obtained with the spectropo-

[1] https://mast.stsci.edu/portal/Mashup/Clients/Mast/Portal.html

Table 1: Journal of photometric observations of HD 210684 (TIC 259017938) with *TESS*.

Sector	BJD (start) (2400000+)	t_{exp} (s)	Background subtraction	SNR flux
15	58711.389832	1426	sky background	16840
16	58738.681763	1426	PCA detrended	16850
56	59825.262653	158	sky background	5690
83	60559.443820	158	sky background	5700

Table 2: Journal of spectropolarimetric observations with ESPaDOnS.

Name	HJD (2400000+)	t_{exp} (s)	SNR Stokes I/V
2555627	59177.70782	880	90/80
2556314	59180.71352	880	420/370
2634276	59459.89670	640	400/360
2690049	59542.68543	640	410/370
2690811	59545.68669	640	400/340
2691267	59547.68653	640	240/210
2776992	59805.12729	880	500/460
2782172	59832.00028	880	500/450
2782907	59835.83241	880	530/480
2783031	59836.97868	880	520/450
2783328	59837.95679	880	510/470
2788523	59868.84363	880	520/470
2875391	60093.10957	880	320/290
2918356	60237.84741	880	410/320
2918718	60238.86927	880	460/340
2919861	60243.78181	880	490/360
2942163	60280.71959	880	480/430
2942721	60282.77044	880	480/430
2950026	60316.68966	880	480/420
3169052	60773.14071	880	430/380
3210624	60896.87912	880	410/360
3252228	61017.75834	880	430/400

larimeter ESPaDOnS to study the pulsation properties of this target, derive its rotation period, and measure the mean longitudinal magnetic field. Photometric and spectropolarimetric observations of HD 210684 are described in Section 2. Results of our analysis and lists of the derived global stellar parameters are presented in Section 3. Discussion follows in Section 4.

2. Observations

2.1. TESS photometry and data reduction

HD 210684 (TIC 259017938) has been observed by *TESS* (Ricker et al. 2015) several times during cycles 2, 5 and 7 of its operation (see Table 1). During each cycle, *TESS* covers approximately half of the sky, divided into 13 sectors. Each sector is monitored for $\sim$ 27.4 d using four wide-field cameras covering $24^\circ \times 24^\circ$ each. Data for each sector includes a few gaps; at least one for telescope rotation and, sometimes, multiple due to bad data.

The 24×24 pixel images of the sky-area around HD 210684 were cut-out from *TESS Full Frame Images* accumulated by *TESS* with the help of specially designed code in *Python* using the *TESS*cut service[2] from MAST. This is a modified version of the code developed by Jonathan Labadie-Bartz that employs utilities of the Lightkurve Python package designed for analysis of *Kepler* and *TESS* data (Lightkurve Collaboration et al. 2018). The reduction procedure is described in detail by Labadie-Bartz et al. (2022, 2023). For each sector (see Table 1), the raw light curve (RLC) of the target was extracted from these 24×24 pixel cut-out images by selecting a proper aperture. This aperture includes only pixels having high enough ratio (around 40) of accumulated signal with respect to the background level to ensure that the selected pixels have gained most of the signal from HD 210684 and to exclude contamination from nearby weak stars.

To remove the sky background and instrumental trends, the Principal Component Analysis (PCA) detrending method with five regressors was used for the data observed with 1426 s cadence in sector 16 (see Table 1). In the case of data observed with 158 s cadence in sectors 56 and 83, and 1426 s cadence in sector 15 the use of the PCA detrending method results in some flux perturbations in the vicinity of observation gaps. Therefore, a simple sky background subtraction method was used to extract the reduced light curve (LC) in sectors 15, 56 and 83 (for more details, see Labadie-Bartz et al. 2022, 2023). Then, the reduced LCs were cleaned for outliers showing more than 4-sigma deviations (where the mean value and standard deviation were calculated for a sliding time window of a given width) and for photometric measurements strongly contaminated by instrumental noise (usually at the beginning or/and at the end of TESS' observation in each sector). To enshure a proper evalution of the mean value and standard deviation for the sliding time window the width of 71300 sec. was used to remove outliers from data in sectors 15 & 16, and of 31600 sec – for data in sectors 56 & 83. The reduced flux and derived respective error-bars were transformed to stellar magnitudes for further analysis.

2.2. Spectropolarimetry with ESPaDOnS

After detection of rotational modulation in the photometric data accumulated by *TESS* for HD 210684 during cycle 2 (sectors 15 & 16) this roAp star was selected for follow-up spectropolarimetric observations with the spectropolarimeter ESPaDOnS (Echelle SpectroPolarimetric Device for Observations of Stars)[3] installed at CFHT. ESPaDOnS uses the deep-depletion e2v device Olapa that allows it to produce high-resolution (R=65000) Stokes I, V, Q & U spectra in the spectral domain from 3700Å to 10000Å. The optical characteristics of the instrument and its performances are described in detail by Donati et al. (2006)[4]. The dedicated package Libre-ESpRIT (Donati et al. 1997) was employed by the CFHT's team to reduce the Stokes I spectra and the Stokes V circular polarisation obtained for HD 210684.

This target has been observed with ESPaDOnS during several semesters starting from the semester 2021B (CFHT) and finishing by the semester 2025B (CFHT). Luckily for us, the acquired high-resolution and high signal-to-noise ratio (SNR) Stokes I & V spectra cover the time interval before and after the time-interval of *TESS* observation of HD 210684 in sectors 56 and 83 (see Tables 1, 2). This fortunate time coverage al-

[2] FFI cutouts and sector information from MAST: https://mast.stsci.edu/tesscut/

[3] CFHT's web page for ESPaDOnS: https://www.cfht.hawaii.edu/Instruments/Spectroscopy/Espadons/

[4] For more details about this instrument, the reader is invited to visit www.cfht.hawaii.edu/Instruments/Spectroscopy/Espadons/

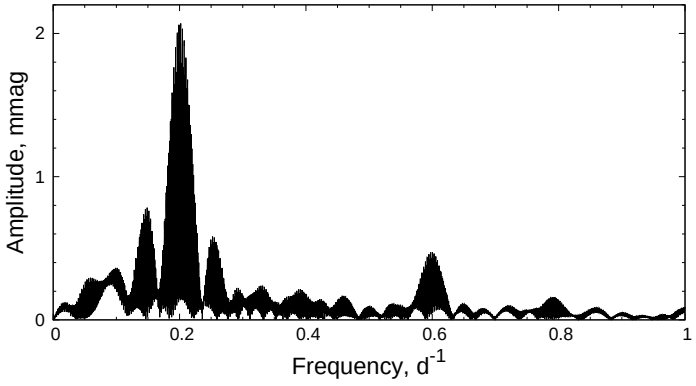

Fig. 1: DFT of the combined photometric data obtained for the low frequency domain. The most prominent signal and its overtones are caused by rotational modulation of the studied LC.

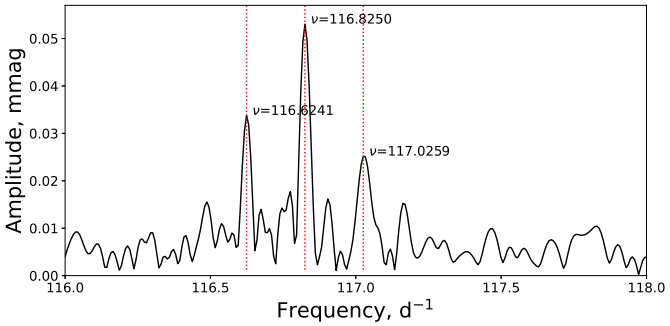

Fig. 2: The same as Figure 1, but for a higher frequency range. Frequencies of the three detected signals (red dotted vertical lines) are split with the rotational frequency which allowed for an improved estimation of the rotational period.

lowed one to measure with high precision the values of rotational phases required for a study of the mean longitudinal magnetic field variability. The first spectrum of the target acquired on HJD= 2459177.70782 has a relatively small SNR (<100, see 4^{th} column in the Table 2) for Stokes I & V spectra at the echelle order #38 centered at 596 nm due to bad weather conditions. Considering that all spectropolarimetric observations of HD 210684 were acquired by ESPaDOnS in the *snapshot mode*, we decided to keep a relatively high exposure time and requested a high SNR per four exposures to obtain its value over 400 even under poor weather conditions.

3. Data analysis

3.1. Study of photometric variability of HD 210684

The reduced data on *TESS* stellar photometry from all four available sectors were combined and analysed with the help of *Period04* software (Lenz & Breger 2005). We have employed the Discret Fourier Transformation (DFT) method to derive frequencies with significant (SNR>4) amplitudes at the low frequency domain (see Fig. 1). Error bars for the resulting frequencies, amplitudes and phases were calculated using the least-square method and Monte-Carlo method, both implemented in *Period04*. The most significant peaks appear at the frequency $\nu_{\rm rot} \simeq 0.199133\,{\rm d}^{-1}$ (P≃5.02177 d) and its second overtone which are most probably caused by rotational modulation of the light curve. To derive the period of stellar rotation with higher precision one can use the frequency of the second overtone frequency $3\nu_{\rm rot}$=0.597386±0.000006 d^{-1} that results in the period of stellar rotation P=5.02188±0.00005 d ($\nu_{\rm rot}$=0.1991286±0.000002 d^{-1}). This period is used to estimate rotational phases for each obtained spectrum (see Table 4).

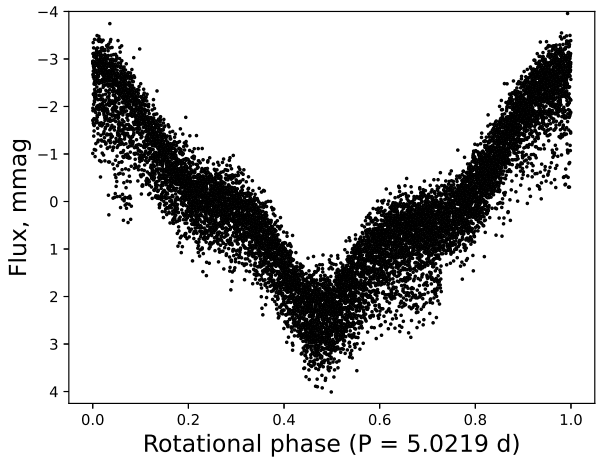

Fig. 3: Light curve of HD 210684 folded with the rotational period according to ephemerides given in the equation (**??**).

The normalized Lomb-Scargle periodogram (VanderPlas 2018) applied to the reduced data from sector 56 has revealed three significant signals (see Fig. 2) that correspond to the roAp type stellar pulsations (for more details, see Kurtz 1982). The three detected signals are split by the frequency $\nu_{\rm split}$=0.2008664±0.0000014 d^{-1} which appears to be similar to the frequency of stellar rotation, but is significantly larger given the error-bars. Apparently, the high-overtone pulsations detected in the LC of HD 210684 are split due to the stellar rotation at the layer of stellar interior where those pulsations are generated. The splitting frequency corresponds to the rotational period of 4.97843±0.00004 d, which is much shorted than the rotational period derived from the most prominent signal in the low frequency domain. This result implies that the stellar interior of HD 210684 rotates faster than its surface, and that we have a clear case of the angular momentum transfer in the studied target (for details see Takahashi & Langer 2021, 2025).

Employing routines available in the code *Period04* we derived phase for the rotation frequency $\nu_{\rm rot}$=0.1991286±0.000002 d^{-1} and recalculated it for the BJD of the start of observations in sector 56. This phase value has then been used as input to *curve_fit*-routine in python to fit the LC phased with the given rotational period by combination of harmonic signals varying with rotation frequency and its second harmonic (see Fig. 1). The *curve_fit*-routine provides a refined phase that corresponds to the maximum of phased flux, BJD of the first such maximum observed in sector 56, and their error-bars. The phased LC is shifted on phase such that the zero-phase corresponds to the maximum detected flux (see Fig. 3). This approach allows us to derive the following

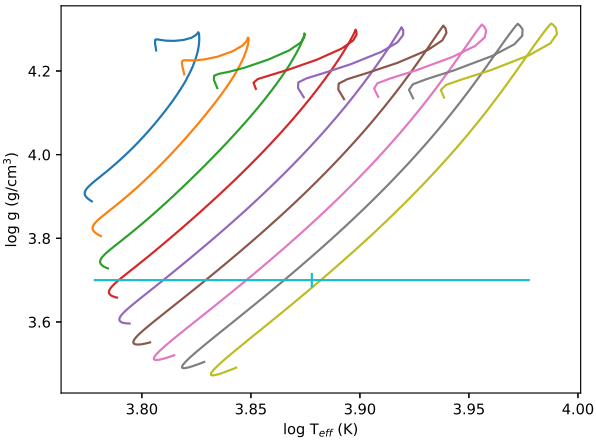

Fig. 4: Evolution tracks for 1.4 - 2.2 $M_\odot$ models in a Kiel diagram. All models in this figure have a rotation rate of 50 km s^{-1} on the ZAMS, and a convective overshoot parameter of $\alpha = 0.02$. The position of HD 210684 is shown, with the errorbars indicating 1σ uncertainties on the observed effective temperature and surface gravity.

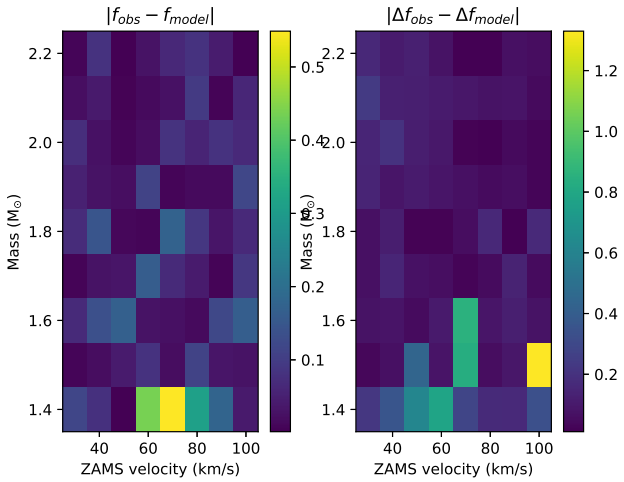

Fig. 5: The difference between the model $\ell = 1$ frequency and observed central frequency (left panel) and the observed and model splitting (right panel) for models with overshoot parameter f_{ov}=0.04. Each point represents an evolution track, and the model that best matches the central frequency has been taken along each track. As expected, there are many possible values based on the central frequency alone, making it hard to constrain this star. The splitting values do rule out some regions of parameter space.

ephemerides for the rotational modulation in HD 210684 :

$E = 2459829.53514 \pm 0.00001 + 5.02188 \pm 0.00005$ BJD,

where the first member specifies BJD for the first LC maximum in sector 56, while the seconde member provides rotational period. Figure 3 shows non-sinusoidal variability with the flux minimum located close to the phase φ=0.45, and some "flat" areas around φ=0.25 and 0.7. A larger dispersion of the flux is usually found at the time intervals close to the observational gaps and is most probably caused by instrument itself.

3.2. Simulation of stellar pulsations

3.2.1. Models

We have calculated a grid of stellar structure and evolution models using MESA version 12778 (Paxton et al. 2011, 2013, 2015, 2018, 2019). The grid covers main sequence models from 1.4 to 2.2 $M_\odot$ in increments of 0.1 $M_\odot$, including the effects of convective overshoot and rotation. Rotation rates varied from 30 km s^{-1} to 100 km s^{-1} on the ZAMS based on the rotational velocity derived from spectroscopy. Convective mixing was calculated using the mixing length theory (Böhm-Vitense 1954) with a mixing length $\alpha = 2.0$. Convective overshoot was included above and below convective zones using the exponential formalism (Herwig 2000) with the overshoot parameter ranging from 0 to 0.04. As discussed below, spectral fitting to the Balmer line profiles provided [M/H]=0 with slight overabundance of α-elements $[\alpha/H] = 0.3 \pm 0.1$, consistent with a metallicity of Z = 0.02, which we have adopted for our model grid. Evolution tracks are shown for $f_{ov} = 0.02$ and $v_{ZAMS} = 50$ km s^{-1} in Figure 4. The observed position of HD 210684 is marked and the errorbars show the 1σ uncertainties on the parameters based on the fits to Balmer lines.

We saved detailed models every 10 time-steps, and used these to calculate linear non-adiabatic pulsation frequencies with GYRE (Townsend & Teitler 2013; Townsend et al. 2018). Since only one frequency triplet is observed, we calculated theoretical frequencies over a small range, from 115 d^{-1} to 118 d^{-1} for

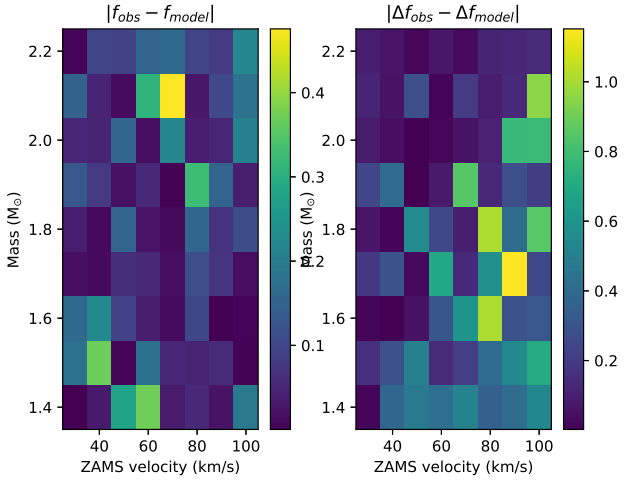

Fig. 6: The same as for Figure 5 for models with $f_{ov} = 0.01$. The region excluded by poor match to the observed splitting becomes much larger at lower overshoot.

$\ell = 1$ and 2, with m = -1, 0, or +1. At each model, we identified the frequency triplet with a central frequency closest to the observed frequency, $\nu = 116.8250$ d^{-1}. Using this triplet, we calculated the absolute value of the difference from the central frequency. The model splitting was calculated using the average of the $(m = 1) - (m = 0)$ and $(m = 0) - (m = -1)$ splitting. The distribution of these two fit parameters are shown for $f_{ov} = 0.04$ in Figure 5.

Mass ($M_\odot$)	Radius ($R_\odot$)	f_{ov}	v_{ZAMS} (km s^{-1})	v_{eq} (km s^{-1})	Age (Gyr)	X_c	ℓ
2.3	3.52	0.0	50	32.1	6.56	0.025	1
1.8	3.07	0.03	40	26.6	1.45	0.223	2

Table 3: Properties of the best-fit models.

3.2.2. Rotational splitting

As shown in Figure 5, with only a single triplet, we can place very limited constraints on the stellar parameters. Matching the splitting does rule out some areas of the parameter space, as can be seen in the right panel of Figure 5. Models with high rotation rates and low mass have splitting that is a poor match to the observations. At lower overshoot parameters, this region becomes much larger, as shown in Figure 6.

Overall, our models favour the higher end of the mass range and lower initial rotation velocities, regardless of overshoot. The vast majority of our fits correspond to evolved main sequence models, and those that are fit to young models using the central frequency tend to be excluded by the fits to the splitting.

With only one observed frequency triplet, we do not expect to be able to tightly constrain the star based on comparison to the theoretical models. To determine our best fitting model, we identified a subset of 223 models where the central frequency of the model triplet was within 0.05 d^{-1} of the observed value. We then determined which of these models showed the lowest difference from the observed splitting. This process was done separately assuming the triplet was an $\ell = 1$ and $\ell = 2$ mode. The best fitting parameters for these two models are summarized in Table 3.

We found that the properties of the best fitting models are consistent with the observed properties of HD 210648. As shown in Figure 7, the best fitting models are within the error bars of the star, with the $\ell = 1$ modes providing a slightly better fit (see Table 3). Nevertheless, the models with $\ell = 2$ result in a better agreement with the found values of the angle between the axis of magnetic dipole and the rotaion axis $\beta = 77° \pm 3°$ (see Subsection 3.5.2), and the equatorial velocity 30.9±0.6 km s^{-1} (see Subsection 3.4).

Finally, we looked at the predicted excitation of the modes in our models, and found that neither of the best fitting models predict excited frequencies in this region. Both models have $\eta \approx -0.9$, indicating the frequencies should be strongly damped throughout their evolution. We looked at the growth rates of all $m = 0$ modes in our grid, and found that the growth rates are only predicted to be positive for some of the coolest models ($\log T_{\rm eff} < 3.85$), as shown in Figure 8. In general, the models that show excitation correspond to the most evolved models in our grid.

3.2.3. Angular momentum transfer

Considering that splitting of high-overton pulsations at the depth of their origin provides rotational period P= 4.97843 ± 0.00004 d, which is significantly smaller then the opriod derived from rotational modulation at the stellar surface (see Subsection 3.1), we used the aforementioned best fit models to study a propbable angular momentum transfer in HD 210684.

In the best fit model with $\ell = 1$ pulsation modes, the driving region posses a temperature of $\log T = 4.04$, which occurs in stellar interior at a radius of 3.52323 ± 0.00003 $R_\odot$. This model corresponds to $M_\star$= 2.3 $M_\odot$ and $R_\star$= 3.52 ± 0.01 $R_\odot$ (see Table 3). In the case of $\ell = 2$ pulsation modes, the driving region is at the layer with $\log T = 4.328$ and located at the distance 3.00332 ± 0.00009 $R_\odot$ from the stellar center. The second best fit model corresponds to $M_\star$= 1.8 $M_\odot$ and $R_\star$= 3.07 ± 0.06 $R_\odot$.

One can deduce that $\ell = 1$ modes are driven at the layers statistically indistingiushable from the stellar surface. In this case, the rotational period derived from the high-overtone triplet should be almost the same as the one found for the stellar surface. Meanwile, the modes with $\ell = 2$ are driven much deeper, at the layer with radius that is statistically different from the stellar radius, and therefore the rotational periods at that layer and the stellar surface can be statistically different as well. This result suggets that best fit model with $\ell = 2$ modes appears to be more plausible because it provides room for an angular momen-

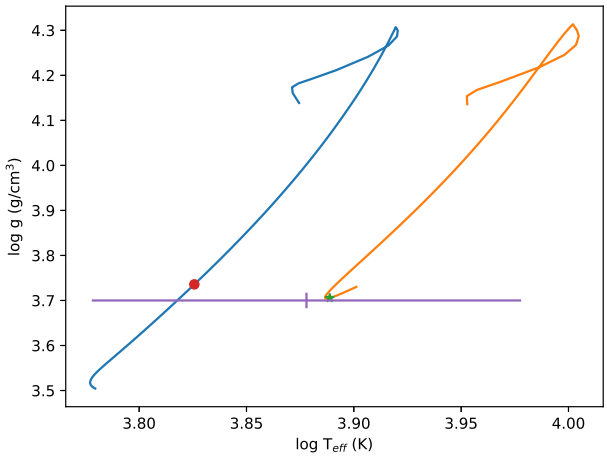

Fig. 7: The Kiel diagram showing the evolution tracks of the two best-fitting models (see Table 3). The observed location of HD 210684 is shown with 1-σ errorbars. The location of the best fitting model based on $\ell = 1$ (green *) and $\ell = 2$ (red ○) are shown.

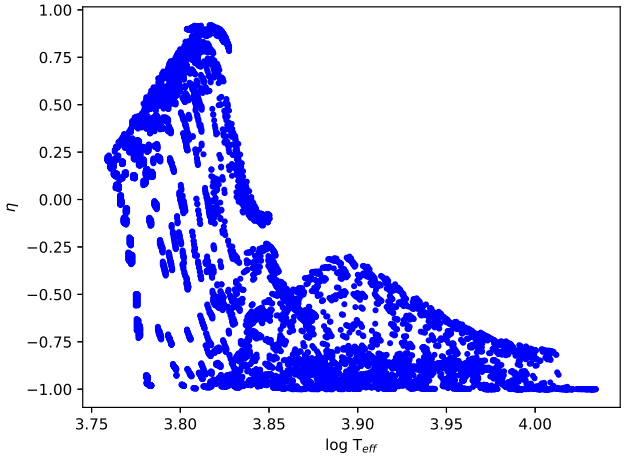

Fig. 8: The predicted growth rates for all $m = 0$ modes in our model grid. Only some of the models with $\log T_{\rm eff} < 3.85$ show positive growth rates.

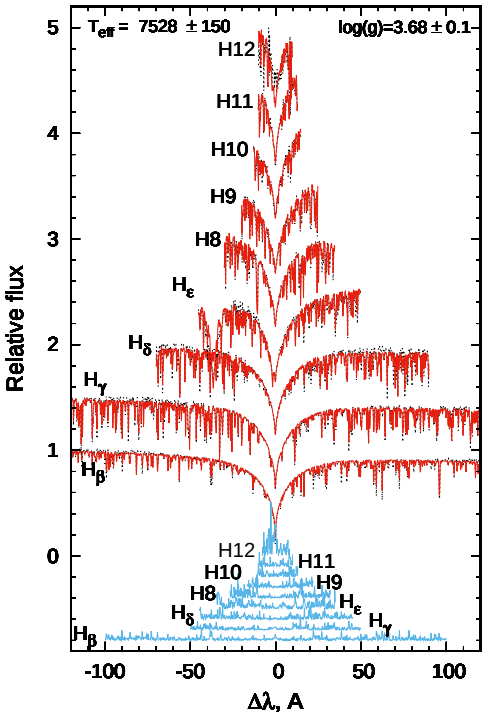

Fig. 9: An example of fitting the observed Balmer line profiles (black dashed line) of HD 210684 by synthetic spectrum (red line) that corresponds to the model of stellar atmosphere with $T_{\rm eff}$ = 7528±150 K, $\log g$ = 3.68±0.1, [M/H]= 0, [α/H]= 0.33±0.1, and to the values of vsin i = 16.0±0.5 km s^{-1}, $v_{\rm r}$= -18.0±0.5 km s^{-1} (χ^2/ν = 0.3255). Differences between the observed and synthetic profiles are shown at the bottom of this image (blue line). The Balmer line profiles are shifted by 0.5 and the differences are shifted by 0.1 for the sake of visibility. The observed spectrum has been obtained on HJD=2460773.14071 that corresponds to the rotational phase φ=0.899 (see Table 4).

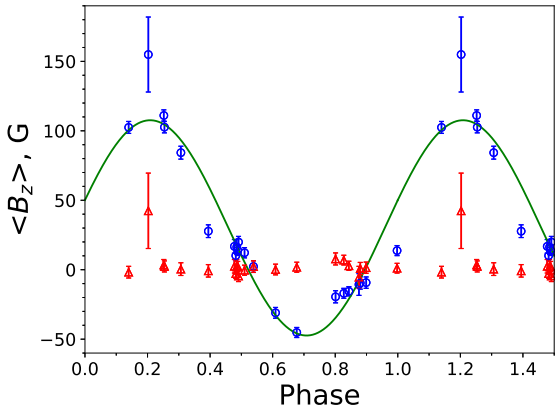

Fig. 10: Variability of the mean longitudinal magnetic field (blue open circles) with the phase of rotational period P=5.02188 d. approximated by the simulated $\langle B_{\rm z}\rangle$-curve (green line) assuming model of the centered magnetic dipole. Red open triangles show level of the possible instrument polarization, $\langle N_{\rm z}\rangle$, inferred from the null profile.

tum transfer from the deeper faster rotating layers to the stellar surface.

3.3. Fitting of Balmer line profiles

From the Stokes I spectra, the observed Balmer line profiles and metal lines in the wings were fit with synthetic profiles calculated by Husser et al. (2013) for stellar atmosphere models with different $T_{\rm eff}$, $\log g$, and abundance of α-elements (O, Ne, Mg, Si, S, Ar, Ca, and Ti) under the condition of solar metallicity for other elements using the code PHOENIX-16 (Hauschildt et al. 1997) and an approach similar to Hauschildt et al. (1999). The code FITSB2 (Napiwotzki et al. 2004) was employed to fit the Balmer line profiles and estimate the values of $T_{\rm eff}$, $\log g$, abundance of α-elements, rotational velocity vsin i, and radial velocity $v_{\rm r}$ of the studied target (see Fig. 9). The abundance of α-elements and metallicity can be derived by fitting metal lines in the wings of the Balmer profiles. Preliminary analysis has shown that the best fit is obtained for [M/H] = 0 when spectral lines of several metals are still strong. Therefore, we have used the abundance of α-elements as a free fitting parameter assuming that the other chemical species have solar abundance. If there is a strong magnetic broadening of the Balmer profiles, the magnitude of $v \sin i$ can be overestimated. However, HD 210684 possesses a relatively weak magnetic field, and the lowest value of vsin i=16.0±0.5 km s^{-1} derived from the analysis of Balmer line profiles coincides with the rotational phase $\varphi \simeq 0.9$, where the mean longitudinal magnetic field $\langle B_{\rm z}\rangle$ is close to zero. Considering that the modul of the measured $\langle B_{\rm z}\rangle$ never exceeds 200 G (see Table 4), we assume here that the weak mean horizontal magnetic field does not contribute substantially to the magnetic broadening.

The best fit values of $T_{\rm eff}$, $\log g$, abundance of α-elements, rotational velocity vsin i, and $v_{\rm r}$ and their associated error-bars based on the fitting of the Balmer line profiles in the Stokes I spectra are shown in Table 4 in the columns 3, 4, 5, 6, and 8 respectively, together with the best fit parameter χ^2/ν in column 9. The corresponding rotational phases in column 2 have been calculated with respect to the derived rotational period P=5.02188 d (see Subsection 3.1) taking into account HJDs (column 1) corresponding to the acquisition time of each analyzed spectrum.

Two different Stokes I spectra acquired on HD 210684 at HDJ = 2460282.77044 and HJD = 2459835.83241 fall in the same rotational phase φ = 0.25 and actually provide very similar estimates of the global stellar parameters. The same is true for the five spectra acquired at HDJ = 2459835.83241, HDJ = 2459836.97868, HDJ = 2460093.10957, HDJ = 2460243.78181, and HJD = 2459832.00028 that correspond to rotational phases close to φ=0.48 – 0.49, and for a pair of spectra acquired at HDJ = 2459547.68653 and HJD = 2459542.68543 that correspond to the phase φ = 0.88. The best fits with the lowest values of χ^2/ν correspond to the rotational phases φ=0.49 and 0.90, where $\langle B_{\rm z}\rangle$ is close to zero. The results obtained for the second phase with the lowest χ^2/ν=0.3255 are shown at Fig. 9. It should be also noted that the largest values of χ^2/ν are derived for φ=0.20 and 0.68, where $\langle B_{\rm z}\rangle$ reaches its extrema.

For the rotational phases φ = 0.14 – 0.39, that correspond to the significant positive $\langle B_{\rm z}\rangle$ measurements (see Fig. 10), the best fit of Balmer line profiles has resulted in a strong overestimation of $T_{\rm eff}$, log(g) and vsin i with relatively high values of the best fit parameter χ^2/ν (see Table 4). The aforementioned phases correspond to the first plateau observed at the phased LC (see Fig. 3). It appears that when the positive magnetic pole is most visible

Table 4: Global stellar parameters of HD 210684 derived from the analysis of Balmer line profiles visible in the acquired spectra (see Table 2) and LSD measurements of the mean longitudinal magnetic field at corresponding rotational phases.

HJD (2400000+)	Rot. phase	$T_{\rm eff}$, K	log(g)	[α/H]	$v_{\rm r}$, km s^{-1} Balmer	$v_{\rm r}$, km s^{-1} LSD	vsin i, km s^{-1}	χ^2/ν	$\langle B_{\rm z}\rangle$, G	$\langle N_{\rm z}\rangle$, G
59805.12729	0.140	7815±150	4.65±0.10	0.36±0.10	-17.1±0.5	-17.3±0.1	20.0±0.5	0.5385	102±4	-2±5
59177.70782	0.202	7784±150	4.47±0.10	0.20±0.10	-18.4±0.5	-18.6±0.1	19.0±0.5	0.6890	155±27	42±27
60282.77044	0.252	7828±150	4.73±0.10	0.35±0.10	-19.2±0.5	-19.4±0.1	19.0±0.5	0.5587	111±4	3±4
59835.83241	0.254	7819±150	4.68±0.10	0.34±0.10	-19.4±0.5	-19.6±0.1	19.4±0.5	0.5379	103±4	2±4
60237.84741	0.307	7784±150	4.65±0.10	0.34±0.10	-19.5±0.5	-19.4±0.1	19.5±0.5	0.4031	84±4	0±4
59459.89670	0.394	7739±150	4.53±0.10	0.34±0.10	-19.6±0.5	-19.4±0.1	17.0±0.5	0.3889	28±5	-1±5
59545.68669	0.478	7581±150	3.67±0.10	0.36±0.10	-19.2±0.5	-19.2±0.1	16.3±0.5	0.3664	17±5	2±5
59836.97868	0.482	7570±150	3.66±0.10	0.35±0.10	-18.8±0.5	-18.8±0.1	16.5±0.5	0.3841	10±4	-3±4
60093.10957	0.485	7534±150	3.67±0.10	0.36±0.10	-18.7±0.5	-18.7±0.1	16.6±0.5	0.3768	16±5	2±5
60243.78181	0.488	7581±150	3.68±0.10	0.37±0.10	-18.9±0.5	-18.9±0.1	16.4±0.5	0.3693	14±4	4±4
59832.00028	0.491	7573±150	3.68±0.10	0.35±0.10	-19.0±0.5	-19.0±0.1	16.4±0.5	0.3533	20±4	-5±4
60238.86927	0.510	7558±150	3.66±0.10	0.37±0.10	-18.1±0.5	-18.1±0.1	16.7±0.5	0.3664	12±4	-0±4
60896.87912	0.539	7559±150	3.67±0.10	0.38±0.10	-18.2±0.5	-18.1±0.1	17.3±0.5	0.3909	2±4	2±4
61017.75834	0.609	7574±150	3.65±0.10	0.42±0.10	-18.4±0.5	-18.4±0.1	18.0±0.5	0.4267	-31±4	0±4
59837.95679	0.677	7553±150	3.65±0.10	0.42±0.10	-18.7±0.5	-18.6±0.1	18.6±0.5	0.4216	-45±4	2±4
59180.71352	0.801	7535±150	3.68±0.10	0.38±0.10	-19.1±0.5	-19.2±0.1	18.2±0.5	0.3670	-19±4	8±4
59868.84363	0.827	7537±150	3.67±0.10	0.35±0.10	-19.1±0.5	-19.3±0.1	17.3±0.5	0.3314	-17±4	7±4
60280.71959	0.844	7551±150	3.67±0.10	0.35±0.10	-19.6±0.5	-19.7±0.1	17.2±0.5	0.3321	-16±3	3±3
59547.68653	0.876	7490±150	3.73±0.10	0.31±0.10	-18.9±0.5	-19.2±0.1	16.7±0.5	0.3512	-11±8	-5±8
59542.68543	0.880	7511±150	3.70±0.10	0.34±0.10	-18.8±0.5	-19.0±0.1	16.7±0.5	0.3335	-10±4	1±4
60773.14071	0.899	7528±150	3.68±0.10	0.33±0.10	-18.0±0.5	-18.2±0.1	16.0±0.5	0.3255	-9±4	1±4
60316.68966	0.998	7561±150	3.67±0.10	0.35±0.10	-15.9±0.5	-16.1±0.1	17.4±0.5	0.3952	14±4	1±4

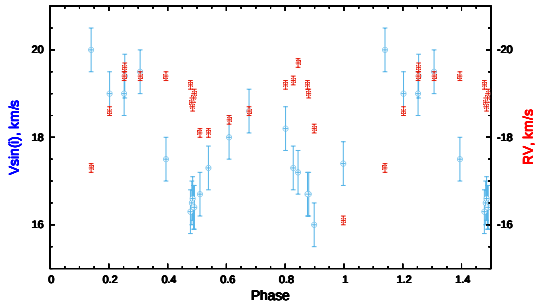

Fig. 11: Variability of LSD radial velocity (red open squares) and vsin i (blue open circles) with rotational phase.

Table 5: Global stellar parameters known and derived for HD 210684 (TIC 259017938).

Parameter	TIC[a]	Gaia[b,c]	This article
$T_{\rm eff}$, K	7568 ± 120	7610^{+10}_{-12}	7550 ± 150
log g	3.87 ± 0.08	3.811±0.005	3.7 ± 0.1
[α/H]			0.3 ± 0.1
$v_{\rm r}$, km s^{-1}			-19.0 ± 0.5
$L_\star$, L$_\odot$	19.27 ± 0.64		
$R_\star$, R$_\odot$	2.55 ± 0.08	2.66 ± 0.13	3.07 ± 0.06
$M_\star$, M$_\odot$	1.76 ± 0.30	2.03 ± 0.10	1.8
age, 10^9 yr			1.45
vsin i, km s^{-1}			16 ± 0.5
$\lvert\langle B_{\rm z}\rangle\rvert$, G			<200
P, days			5.02188±0.00005
$v_{\rm eq}$, km s^{-1}			30.9 ± 0.6
i			31.2° ± 1.8°
β			77° ± 3°

Notes: [a]Stassun et al. (2018, 2019), [b]DR3: Fouesneau et al. (2022), [c]DR2: Kervella et al. (2019).

in HD 210684 around φ = 0.20, one can also see a "hot spot" in its vicinity towards the stellar equator that contributes to our measurements of $T_{\rm eff}$ and log(g). This hypothesis is supported by the measured radial velocity that changes significantly in this phase interval from -17 km s^{-1} to -19.5 km s^{-1}, while the vsin i reaches its maximum values (see Fig. 11), suggesting that the "hot spot" appears at φ = 0.0, crosses the central meridian of the star around φ= 0.20, and contributes to widening of observed Balmer line profiles. Nevertheless, to have a clearer picture and explain why the maximum of the derived LC appears at φ= 0.0 we need to acquire more spectra around this rotational phase.

Considering the high derived values of χ^2/ν for the best fits in the phase interval φ=0.14 – 0.39 and that our simulation of stellar pulsations in HD 210684 argues in favor of coolest models with log $T_{\rm eff}$ < 3.85 (see Subsection 3.2.2) we used data from other rotational phases to derive proper values of $T_{\rm eff}$= 7550 ± 150 K and log(g)=3.7. The best fits obtained for the Balmer line profiles in all phases shows slightly enhanced abundance of α-elements [α/H]~0.35 assuming the solar abundance for other chemical species.

3.4. Global stellar parameters

Using the stellar radius found for HD 210684 by Kervella et al. (2019) and the value of rotational period (see Subsection 3.1)

one can estimate the equatorial velocity from

$$v_{\rm eq} = \frac{50.5927 R_\star}{P}, \quad (1)$$

where the stellar radius is measured in $R_\odot$, which is recommended by the XXIXth International Astronomical Union (IAU) General Assembly in 2015 to be 695700 km (Prša et al. 2016), and the period is measured in days. The resulting value for equatorial velocity is 30.9±0.6 km s^{-1} (see Table 5), and, in combination with the most probable value of vsin i=16 km s^{-1} derived from the fitting of Balmer line profiles, it results in an angle $i = 31.2° \pm 1.8°$ that specifies inclination of the rotational axis to the line of sight.

Blomme et al. (2022) have shown that the template parameters $T_{\rm eff}$, log g, and [M/H] (Fouesneau et al. 2022) used by CU6 are not necessarily a good description of the spectral type of the star in he Gaia DR3 archive. Nevertheless, the values of $T_{\rm eff}$ and log g derived in this study from the best fit of Balmer line profiles (see Subsection 3.3) are in good accordance with the data found in TESS Imput Catalogue (TIC) (Stassun et al. 2018, 2019) and Gaia DR3 archive (Fouesneau et al. 2022) considering the error-bars. The effective temperature determined here, $T_{\rm eff} = 7550 \pm 150$ K, is close to the upper limit found for $T_{\rm eff}$ from the analysis of stellar pulsations.

Considering that the obtained equatorial velocity 30.9±0.6 km s^{-1} and the angle $\beta = 77° \pm 3°$ between the rotation and dipolar exes (see Subsection 3.5.2) better describe the amplitude ratios for the observed pulsation triplet in the best fit model with $\ell = 2$ modes (see Subsection 3.1), we have derived probable age of HD 210684 to be around 1.45 Gyr (see Table 3). Its stellar mass $M_\star$= 1.8 $M_\odot$ and radius $R_\star$= 3.07 $R_\odot$ derived from the simulation of stellar pulsations (see Subsection 3.2.3) are in good accordance with the data provided by TIC (Stassun et al. 2018, 2019), and Gaia DR3 (Fouesneau et al. 2022) archives (see Table 5).

3.5. Magnetic field evaluation

3.5.1. Oblique pulsator model

The normalized Lomb-Scargle periodogram calculated for the region of high frequencies (see Fig. 2) also provides the amplitudes of high-overtone pulsations that can be used in the frame of oblique pulsator model (OPM) (Kurtz 1982) to estimate the angle β between the axis of magnetic dipole and the rotation axis. One should always pay attention to the property of Lomb-Scargle periodogram, where the amplitude of detected signals is a function of time sampling in the original LC see for details VanderPlas (for details see 2018), but this estimate of β can be considered as a preliminary value. Following the frequency analysis performed by Handler et al. (2006) for HD 99563 one can apply the OPM that provides a relation for pulsation modes with ℓ=1 (Shibahashi 1986):

$$\frac{A^{(1)}_{+1} - A^{(1)}_{-1}}{A^{(1)}_0} = \sin\beta \sin i, \quad (2)$$

where $A^{(1)}_0$ is the amplitude of the central frequency in the high-overtone triplet, $A^{(1)}_{+1}$ and $A^{(1)}_{-1}$ are, respectively, the amplitudes of the higher and lower rotational side-lobes, and i specifies angle between the line of sight and the rotational axis of the star. For the derived amplitudes of high-overtone pulsations equation (2) results in $\sin\beta \sin i = -0.13^{+0.13}_{-0.19}$. Considering the known angle $i = 31.2° \pm 1.8°$ (see Table 5) one can derive that the angle β is relatively small or close to zero ($\beta \simeq -14^{\circ}{}^{+14^\circ}_{-37^\circ}$).

If the observed triplet of high-overtone pulsations consists of modes with ℓ=2 one should employ the following relation (Kurtz 1992; Shi et al. 2021):

$$\frac{A^{(2)}_{+1} + A^{(2)}_{-1}}{A^{(2)}_0} = \frac{12 \sin\beta \cos\beta \sin i \cos i}{(3\ cos^2\beta - 1)(3\ sin^2 i - 1)}, \quad (3)$$

where $A^{(2)}_0$ is the amplitude of the central frequency, $A^{(2)}_{+1}$ and $A^{(2)}_{-1}$ are, respectively, the amplitudes of the higher and lower rotational side-lobes. For the known angle i this relation can be transformed into a quadratic equation with respect to cos (2β) and solved analytically:

$$cos(2\beta) = \frac{-3\ b^2 \pm 4\ a \sqrt{2\ b^2 + a^2}}{9\ b^2 + 4\ a^2}, \quad (4)$$

where

$$a = 6\ sini \cos i, \quad b = \frac{A^{(2)}_{+1} + A^{(2)}_{-1}}{A^{(2)}_0}(3\ sin^2 i - 1).$$

For the derived value of angle i the equation (4) provides $\beta \sim 0°$ (for positive sign in front of the square root) and $\beta \sim 90°$ (for negative sign). Clearly the error bars are large in this case, and no constraints can be placed on the magnetic field orientation.

3.5.2. Measurement of the mean longitudinal magnetic field

Normalized Stokes I & V spectra of HD 210684 have been used to calculate the LSD profile (Donati et al. 1997; Kochukhov et al. 2010) and to measure $\langle B_z \rangle$ with the help of SpecpolFlow software (Erba 2024; Folsom et al. 2025). This code[5] was initially developed by Dr. Colin Folsom to analyse data provided by spectropolarimeters ESPaDOnS and Neo-NARVAL (or by NARVAL in the past), and is currently updated and supported by the SpecpolFlow team developers in the framework of the MOBSTER collaboration.[6]

To calculate LSD profiles we created line-masks compiled from the list of atomic data for spectral lines inferred from the VALD3 database (Piskunov et al. 1995; Kupka et al. 1999, 2000) for our target with $T_{\rm eff}$=7550 K, log(g)=3.7 and [M/H]=0.0 (see Tables 4, 5) assuming microturbulence velocity $v_{\rm mic}$= 2 km s^{-1} in the spectral domain from 3700Å to 9500Å. The first mask contains data for 7404 lines that belong to different chemical species, while the second list of lines with high Lange factor (>1.2) includes only 3316 entries. Considering that the derived vsin i= 16.0 km s^{-1} we adopted LSD width of 20 km s^{-1} to calculate the mean longitudinal magnetic field. The use of two different line-masks results in almost the same $\langle B_z \rangle$ values, but we report here only the data obtained with the line-mask containing solely lines with the high Lange factor because the final error-bars appear to be more realistic as compared to the measurement of polarized signal $\langle N_z \rangle$ from the null profiles (see Fig. 10). Corresponding radial velocities were derived from the fitting LSD Stokes I profiles by Gaussian function (see column 7 for LSD v_r in Table 4). For each studied rotational phase, they are in a good accordance with the radial velocities derived from the fitting of Balmer line profiles.

[5] https://folsomcp.github.io/specpolFlow/index.html
[6] https://mobster-collab.com/

Figure 10 presents the obtained $\langle B_z \rangle$ values that show clear variability with the rotational period P=5.02188 d derived from the *TESS* photometry. The mean longitudinal magnetic field reaches its maximum at the rotational phase φ= 0.21 which is shifted with respect to the maximum on the phased LC at φ= 0.0 (see Fig. 3). Unfortunately, the measured $\langle B_z \rangle$ maximum has the largest error-bar because it corresponds to the spectrum with the lowest SNR (see Table 2). The minimum of $\langle B_z \rangle$ with significant field is found around the phase $\varphi \sim 0.68$ that corresponds to the second plateau on the phased LC observed after the minimum (see Fig. 3). The employed LSD method provides quite small values of the significant mean longitudinal magnetic field, which is less than 200 G in its maximum.

In the case of centered magnetic dipole the oblique magnetic rotator (OMR) model provides the following expression (see Babcock 1958; Mathys 1988; Bagnulo et al. 1996; Khalack 2002, for more detail):

$$\langle B_z \rangle \simeq B_p(\cos\beta\cos i + \sin\beta\sin i\cos(\varphi + \varphi_0)), \quad (5)$$

to approximate the measured $\langle B_z \rangle$ variability with a theoretical curve (see green line in Fig. 10). Here, B_p specifies intensity of the surface magnetic field at the magnetic pole, and φ_0 is the phase shift, in the case $\langle B_{z,max} \rangle$ does not appear at $\varphi = 0$. We can see that the positive magnetic pole is most visible at the rotational phase $\varphi \sim 0.21$, while the negative magnetic pole appears around $\varphi \sim 0.68$. From the fitting (using the *curve_fit* routine from python's scipy.optimize[7] library) mean longitudinal magnetic field measurements phased with the rotational period we derived the angle between dipole and rotation axes $\beta = 77° \pm 3°$ for the known inclination of the rotation axis to the line of sight $i = 31.2° \pm 1.8°$. The fact that the derived approximation does not fit well at all $\langle B_z \rangle$ measurements indicates that the real surface magnetic field structure is different from the dipolar configuration, and higher multipoles (Bagnulo et al. 1996) or a decentered magnetic dipole (Khalack 2002, 2005) should be considered.

3.6. Rotational variability of the observed LSD line profiles

The LSD Stokes I & V profiles simulated for each spectropolarimetric data of HD 210684 (see Subsection 3.5.2) were phased with the rotational period to study their variability that could contain information about a horizontal abundance stratification of different chemical species. No matter that the derived $\langle B_z \rangle$ is very weak, the simulated LSD Stokes V & I profiles show clear variability with the rotational phase (see Fig. 12).

Figure 12 demonstrates that for similar rotational phases derived LSD Stokes I & V profiles appear to be almost identical (see, for example, φ = 0.25, 0.48-0.49, 0.88, etc.), no matter that those spectra were obtained at the very different HJD. The time span between our first and last spectropolarimetric observation of HD 210684 is 1840 days. Meanwhile, at the rotational phase φ = 0.876-0.880, the LSD Stokes I & V profiles are almost the same for two spectra obtained in a time span of 5 days (see Table 4). These results argue in favour of a proper determination of rotational period with respect to the available data of *TESS* photometry.

The simulated LSD Stokes I profiles show significant asymmetry at the next intervals of rotational phases φ= 0.25 – 0.39 and 0.80 – 1.00, suggesting that an horizontal stratification of chemical abundance (and respectively of surface temperature) is most pronounced at these phases. The strongest asymmetry of the LSD Stokes I profile is observed at φ= 0.307 and 0.394,

[7] https://docs.scipy.org/doc/scipy/reference/optimize.html

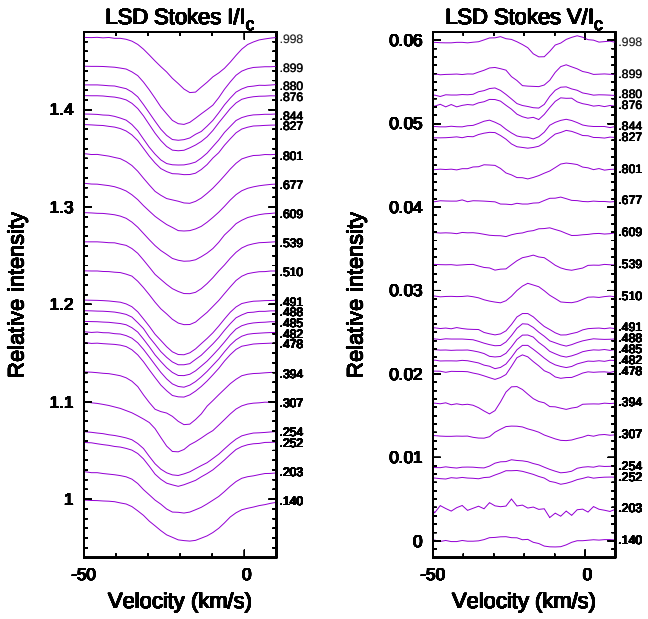

Fig. 12: Variability of the LSD Stokes I (left) and V (right) profiles with rotational phase. LSD profiles are shifted vertically with the rotational phase for the sake of visibility, but those shifts remain small for the same of similar phases.

where the radial velocity remains constant, vsin i and $\langle B_z \rangle$ drop down, and the phased LC also decreases after passing the first plateau (see Figs. 3, 10 and 11). The observed variability and asymmetry of the LSD Stokes I profiles indicates a presence of horizontal abundance stratification in stellar atmosphere of HD 219684. Almost constant (considering error bars) abundance of α-elements measured at different rotational phases may argue for a complex structure of this stratification.

4. Discussion

A detailed analysis of the TESS light curve for HD 210684 in sectors 56 & 83 revealed a triplet of high-overtone pulsations around the frequency ν_p=116.825 d^{-1} that confirms its classification as a roAp type variable (Holdsworth et al. 2024). We have revealed a signal at the range of lower frequencies that corresponds to the rotational modulation of the light curve. The presence of the second overtone of the rotation frequency allowed us to estimate the corresponding rotational period, P=5.02188±0.00005 d. Considering the estimated error bar the rotational period derived in this work appears to be slightly lower than the one reported by Balona (2022) for HD 210684. Assuming that frequencies of the observed triplet of high-overtone pulsations are split by $\Delta\nu$=0.200866 d^{-1} (P= 4.97843±0.00004 d) due to stellar rotation at the layer with radius 3.00332 ± 0.00009 $R_\odot$, where the observed pulsation instability is driven, the stellar interiors rotate significantly faster than the layer at stellar surface ($R_\star$ = 3.07±0.06$R_\odot$). This implies that HD 210684 shows evidence of angular momentum transfer (see Subsection 3.2.3).

Comparison of the observed mode triplet with model frequencies calculated using MESA and GYRE provide some constraints on the stellar parameters ($\log T_{\rm eff} < 3.85$), but are not able to tightly constrain the star. We find our best fitting model depends on whether the observed modes are $\ell = 1$ or $\ell = 2$, and

predict either a higher mass and a low overshoot or a lower mass and a high overshoot. Both of the best fit models are in good agreement with the observed $\log T_{eff}$ and $\log g$ of the star. Considering that the modes with $\ell = 2$ result in the angle $\beta \sim 90°$ between axes of magnetic dipole and stellar rotation is similar to $\beta = 77° \pm 3°$ derived under the assumption of OMR model from the observed variability of the mean longitudinal magnetic field, the preferences should be given to models with $\ell = 2$ modes. However, we find that very few of the models in our grid are predicted to have driven frequencies in the range of observed frequency triplet. Only the most evolved, coolest models show values of $\eta > 0$. It should be noted that our simulation were carried out without considering impuct from a weak magnetic field or probable angular momentum transfer.

Our estimates of the global stellar parameters derived from fitting Balmer line profiles observed in ESPaDOnS spectra are in good agreement with the data inferred from TIC (Stassun et al. 2018, 2019) and DR3 (Fouesneau et al. 2022) archives (see Table 5). Using the stellar radius provided for HD 210684 by Kervella et al. (2019), its rotational period and vsin i derived in this study we estimated the equatorial velocity (see Eq. 1) and the angle of inclination of the rotation axis to the line of sight $i = 31.2° \pm 1.8°$. Giving preferences to the model with $\ell = 2$ modes one can see that HD 210684 continues its evolution on the main sequence (see Fig. 7) having age 1.45 Gyr.

Application of the LSD approach to the normalized Stokes I & V spectra resulted in detection of the mean longitudinal magnetic field that varies with the derived period of stellar rotation on its surface. It reaches its maximum at φ= 0.20 that corresponds to the beginning of a plateau on the phased LC (see Subsection 3.5.2). The derived $\langle B_z \rangle$ measurements are quite small (< 200 G), but significant at the rotational phases when positive or negative magnetic poles are most visible. Variability of the $\langle B_z \rangle$ measurements phased with the rotational period appear to be different from the curve predicted by the OMR model of a centered magnetic dipole (see Fig. 10) suggesting that configuration of the surface magnetic field in HD 210684 is more complex than the dipolar one.

Preliminary analysis of the obtained spectra does not reveal any spectral lines that may belong to a secondary component. HD 210684 might be a probable member of binary system, but the contribution of secondary component to the acquired spectra is negligible which agrees well with the predicted low mass of the secondary (Kervella et al. 2019). This fact suggests that all detected variability of the simulated LSD I profiles (see Fig. 12) is caused by inhomogeneous horizontal distribution of elements abundance in stellar atmosphere of the primary component, which is a weakly magnetic CP star and roAp variable. Considering that the best fit of Balmer line profiles in the spectra aquired for φ= 0.14 – 0.39 results in significantly higher values of $T_{\rm eff}$, $\log(g)$ and vsin i, we assume that a "hot" spot visible at the aforementioned rotational phases may contribute to these effects. This hypotesis is supported by strong asymmentry of the simulated LSD I profile at φ= 0.307 and 0.394 suggesting a link between the location of "hot" spot and patches of enhanced (or depleted) abundance for several chemical species.

As we do not have good coverage of all rotational phases with spectropolarimetric observations, additional high-SNR spectra of HD 210684 are required to carry out detailed mapping of the horizontal abundance stratification for different chemical species and reconstruction of the surface magnetic field configuration. These advanced procedures can help understand better the physics and relations between the unique properties found in HD 210684 in this study. The combination of a weak ($\langle B_z \rangle$ < 200G) and significantly non-dipolar magnetic field, the presence of an area with hotter local surface temperature, a complex structure of horizontal abundance stratification, relatively strong high-overtone pulsations of roAp type, and probable angular momentum transfer make this a fascinating target for future study. A comprehensive study of its nature will provide observational constraints for theoretical simulation of magnetic field generation in magnetic CP stars (Schleicher et al. 2023), its impact to the horizontal and vertical abundance stratification of chemical elements (Alecian & Stift 2021; Alecian 2023) and for GYRE models used to calculate driven frequencies of high-overtone pulsations in roAp stars.

Acknowledgements. V.K. acknowledges support from Mitacs, ACFAS, and is thankful to the Faculté des Études Supérieures et de la Recherch and to the Faculté des Sciences de l'Université de Moncton for financial support of this research. CCL acknowledges support from the Natural Sciences and Engineering Research Council of Canada (NSERC). The authors are grateful to Dr. Holdsworth and Dr. Kochukhov for useful advices that helped to improve this article. The analysed spectra have been obtained at the Canada-France-Hawaii Telescope (CFHT) which is operated by the National Research Council of Canada, the Institut National des Sciences de l'Univers of the Centre National de la Recherche Scientifique of France, and the University of Hawaii. The operations at the Canada-France-Hawaii Telescope are conducted with care and respect from the summit of Maunakea which is a significant cultural and historic site. Author thanks to Oleksandr Kobzar for sharing his spectra for HD 210684 and to the *TESS* and TASC/TASOC teams for their support of the present work. This paper includes data collected by the *TESS* mission. Funding for the *TESS* mission is provided by the NASA Explorer Program. This research has made use of the SIMBAD database, operated at CDS, Strasbourg, France. Some of the data presented in this paper were obtained from the Mikulski Archive for Space Telescopes (MAST) and Gaia DR3 catalogue.

References

Alecian, G. 2023, MNRAS, 519, 5913
Alecian, G. & Stift, M. J. 2021, MNRAS, 504, 1370
Babcock, H. W. 1958, ApJ, 128, 228
Bagnulo, S., Landi Degl'Innocenti, M., & Landi Degl'Innocenti, E. 1996, A&A, 308, 115
Balona, L. A. 2022, MNRAS, 510, 5743
Blomme, R., Fremat, Y., Sartoretti, P., et al. 2022, arXiv e-prints, arXiv:2206.05486
Böhm-Vitense, E. 1954, ZAp, 34, 209
Brandt, T. D. 2021, ApJS, 254, 42
Cannon, A. J. & Pickering, E. C. 1993, VizieR Online Data Catalog, III/135A
Donati, J. F., Catala, C., Landstreet, J. D., & Petit, P. 2006, in Astronomical Society of the Pacific Conference Series, Vol. 358, Solar Polarization 4, ed. R. Casini & B. W. Lites, 362
Donati, J. F., Semel, M., Carter, B. D., Rees, D. E., & Collier Cameron, A. 1997, MNRAS, 291, 658
Erba, C. 2024, in American Astronomical Society Meeting Abstracts, Vol. 243, American Astronomical Society Meeting Abstracts, 225.03
Folsom, C. P., Erba, C., Petit, V., et al. 2025, arXiv e-prints, arXiv:2505.18476
Fouesneau, M., Frémat, Y., Andrae, R., et al. 2022, arXiv e-prints, arXiv:2206.05992
Handler, G., Weiss, W. W., Shobbrook, R. R., et al. 2006, MNRAS, 366, 257
Hauschildt, P. H., Allard, F., Ferguson, J., Baron, E., & Alexander, D. R. 1999, ApJ, 525, 871
Hauschildt, P. H., Baron, E., & Allard, F. 1997, ApJ, 483, 390
Herwig, F. 2000, A&A, 360, 952
Holdsworth, D. L., Cunha, M. S., Kurtz, D. W., et al. 2021, MNRAS, 506, 1073
Holdsworth, D. L., Cunha, M. S., Lares-Martiz, M., et al. 2024, MNRAS, 527, 9548
Husser, T. O., Wende-von Berg, S., Dreizler, S., et al. 2013, A&A, 553, A6
Kervella, P., Arenou, F., Mignard, F., & Thévenin, F. 2019, A&A, 623, A72
Khalack, V. R. 2002, Kinematika i Fizika Nebesnykh Tel, 18, 553
Khalack, V. R. 2005, A&A, 429, 677
Kochukhov, O., Makaganiuk, V., & Piskunov, N. 2010, A&A, 524, A5
Kupka, F., Piskunov, N., Ryabchikova, T. A., Stempels, H. C., & Weiss, W. W. 1999, A&AS, 138, 119
Kupka, F. G., Ryabchikova, T. A., Piskunov, N. E., Stempels, H. C., & Weiss, W. W. 2000, Baltic Astronomy, 9, 590
Kurtz, D. W. 1982, MNRAS, 200, 807
Kurtz, D. W. 1992, MNRAS, 259, 701

Labadie-Bartz, J., Carciofi, A. C., Henrique de Amorim, T., et al. 2022, AJ, 163, 226
Labadie-Bartz, J., Hümmerich, S., Bernhard, K., Paunzen, E., & Shultz, M. E. 2023, A&A, 676, A55
Lenz, P. & Breger, M. 2005, Communications in Asteroseismology, 146, 53
Lightkurve Collaboration, Cardoso, J. V. d. M., Hedges, C., et al. 2018, Lightkurve: Kepler and TESS time series analysis in Python, Astrophysics Source Code Library
Mathys, G. 1988, A&A, 189, 179
Mathys, G., Khalack, V., Kobzar, O., LeBlanc, F., & North, P. L. 2023, A&A, 670, A72
Napiwotzki, R., Yungelson, L., Nelemans, G., et al. 2004, Astronomical Society of the Pacific Conference Series, Vol. 318, Double degenerates and progenitors of supernovae type Ia, ed. R. W. Hilditch, H. Hensberge, & K. Pavlovski, 402–410
Paxton, B., Bildsten, L., Dotter, A., et al. 2011, ApJS, 192, 3
Paxton, B., Cantiello, M., Arras, P., et al. 2013, ApJS, 208, 4
Paxton, B., Marchant, P., Schwab, J., et al. 2015, ApJS, 220, 15
Paxton, B., Schwab, J., Bauer, E. B., et al. 2018, ApJS, 234, 34
Paxton, B., Smolec, R., Schwab, J., et al. 2019, ApJS, 243, 10
Piskunov, N. E., Kupka, F., Ryabchikova, T. A., Weiss, W. W., & Jeffery, C. S. 1995, A&AS, 112, 525
Prša, A., Harmanec, P., Torres, G., et al. 2016, AJ, 152, 41
Ricker, G. R., Winn, J. N., Vanderspek, R., et al. 2015, Journal of Astronomical Telescopes, Instruments, and Systems, 1, 014003
Schleicher, D. R. G., Hidalgo, J. P., & Galli, D. 2023, A&A, 678, A204
Shi, F., Kurtz, D. W., Holdsworth, D. L., et al. 2021, MNRAS, 506, 5629
Shibahashi, H. 1986, in Hydrodynamic and Magnetodynamic Problems in the Sun and Stars, ed. Y. Osaki, 195
Stassun, K. G., Oelkers, R. J., Paegert, M., et al. 2019, AJ, 158, 138
Stassun, K. G., Oelkers, R. J., Pepper, J., et al. 2018, AJ, 156, 102
Takahashi, K. & Langer, N. 2021, A&A, 646, A19
Takahashi, K. & Langer, N. 2025, A&A, 696, A129
Townsend, R. H. D., Goldstein, J., & Zweibel, E. G. 2018, MNRAS, 475, 879
Townsend, R. H. D. & Teitler, S. A. 2013, MNRAS, 435, 3406
VanderPlas, J. T. 2018, ApJS, 236, 16